CSIAM Trans. Life Sci.
doi: 10.4208/csiam-ls.SO-2025-0032

Vol. **x**, No. x, pp. 1-27
xx 2026

BRIDGE: An Interpretable Framework for Transcriptome-Scale Completion of Panel-Limited Spatial Transcriptomics

Bo-Han Si[1], Shi-Tong Yang[1], Meng-Guo Wang[1], Ke Jin[1,2],
Li-Wei Wang[1] and Xiao-Fei Zhang[1,3,*]

[1] *School of Mathematics and Statistics, and Hubei Key Laboratory of Mathematical Sciences, Central China Normal University, Wuhan 430079, China.*
[2] *Institute of Applied Mathematics, Shenzhen Polytechnic University, Shenzhen 518055, China.*
[3] *Key Laboratory of Nonlinear Analysis & Applications (Ministry of Education), Central China Normal University, Wuhan 430079, China.*

Received 2 December 2025; Accepted 1 February 2026

Abstract. Imaging-based spatial transcriptomics provides single-cell resolution but is restricted to targeted gene panels, leaving most transcriptional variation unexplored. Existing imputation approaches often rely on latent-space alignment, which can distort biological structure and capture limited within-type heterogeneity. We present BRIDGE, an interpretable framework that expands panel-limited spatial transcriptomics to transcriptome-level resolution through anchor-guided linear calibration and multi-scale neighborhood-based prediction. BRIDGE learns a global calibration matrix that directly adjusts shared-gene expression between technologies and provides explicit gene-level interpretability. Using the calibrated reference, BRIDGE predicts unmeasured genes by integrating multi-scale local neighborhoods to achieve both accuracy and robustness. Across seven datasets from CosMx, MERFISH, Xenium and multiple tissues and species, BRIDGE exceeds or matches existing methods on gene-level and cell-level accuracy. The calibration matrix offers clear biological interpretation, and the completed transcriptomes recover fine-scale spatial patterns such as cortical lamination and support refined characterization of cell-state heterogeneity, including B-cell states and Stromal subtypes in human breast cancer. BRIDGE provides a robust and interpretable solution for extending imaging-based spatial transcriptomics to transcriptome-scale analysis and enables deeper investigation of microenvironment-dependent cellular programs.

AMS subject classifications: 92B20, 92-08

Key words: Spatial transcriptomics, scRNA-seq, gene expression prediction, interpretability.

---

[*] Corresponding author. *Email address:* `zhangxf@ccnu.edu.cn` (X.-F. Zhang)

1 Introduction

Spatial transcriptomics (ST) technologies integrate gene expression profiling with spatial localization, enabling systematic analysis of tissue architecture and cellular organization [32, 39]. Current ST platforms fall into sequencing-based and imaging-based categories. Sequencing-based approaches such as ST [50], 10x Visium, and Slide-seq [51] provide relatively unbiased transcriptome-wide coverage from spatially barcoded regions but typically operate at lower spatial resolution and may suffer from RNA diffusion and spot mixing. Imaging-based methods, including MERFISH [10], seqFISH [15], Xenium [26], and CosMx [24], use iterative fluorescent imaging with barcoded probes to reach single-cell or subcellular resolution and capture transcript distributions within intact tissues.

Although imaging-based technologies provide high spatial precision, their multiplexing capacity is limited by technical and cost constraints. The gene panels used in these assays are typically derived from single-cell RNA sequencing (scRNA-seq) marker sets and therefore cover only a fraction of the transcriptome [12, 75]. As a result, many spatially regulated programs and fine-grained cellular states cannot be directly observed, creating a need for computational methods that accurately impute unmeasured genes and expand the biological insights obtainable from imaging-based ST [13, 29, 39, 73].

Most existing imputation methods follow a two-stage framework. In the first stage, spatial data and single-cell references are projected into a shared latent space to identify transcriptionally similar cells [2, 11, 23, 33]. In the second stage, expression values for unmeasured genes are estimated by aggregating reference profiles using similarity-based weights. This strategy is effective for recovering broad cell-type identities, but it also introduces several intrinsic limitations. Projection into a latent space can distort local neighborhood structure by altering distances among cells. As a result, biologically distinct cells may appear similar, obscuring within-type variability. Cross-modal alignment may further mix signals from different technologies, reducing the biological plausibility of the inferred neighbors. In addition, most approaches offer limited interpretability and do not clearly distinguish genuine biological signals from alignment-induced artifacts [35]. Together, these issues reflect a structural trade-off in latent-space alignment, where empirical matching accuracy is often achieved at the cost of preserving biological geometry and gene-level interpretability. These limitations can hinder accurate gene imputation and complicate downstream analyses.

To address these limitations, we introduce BRIDGE, an interpretable imputation framework that reframes spatial gene prediction as a structure-preserving cross-modal calibration problem. Rather than relying on latent-space alignment, BRIDGE performs anchor-guided linear alignment directly in gene-expression space, explicitly preserving local expression geometry while yielding an interpretable gene-gene calibration matrix. After calibration, unmeasured genes are predicted by aggregating reference profiles using neighborhood weights that preserve local expression patterns. By decoupling cross-modal calibration from latent embedding and performing prediction on a geometry-preserving representation, BRIDGE mitigates latent distortion, reduces cross-modality mixing, and improves interpretability compared with existing approaches. Across diverse technologies, species, and tissues, BRIDGE surpasses or matches five state-of-the-art methods on both gene-level and cell-level metrics. Applications to MERFISH mouse primary motor cortex and Xenium human breast cancer datasets further demonstrate that the method recovers spatially coherent expression programs and refines cellular subtype structure, underscoring its ability to deepen biological insight from panel-limited spatial assays.

2 Methods

2.1 Overview of BRIDGE

BRIDGE is an interpretable computational framework designed to expand imaging-based spatial transcriptomics from targeted gene panels to transcriptome-level resolution by leveraging a matched scRNA-seq reference, while explicitly preserving gene-expression geometry during cross-modal calibration. The framework integrates two key components: an anchor-guided linear calibration performed directly in gene-expression space, and a multi-scale neighborhood-based imputation strategy. Together, these modules yield an explicit gene-gene calibration matrix and biologically grounded reference neighborhoods that reveal how information is transferred across modalities.

Given a spatial transcriptomics dataset measured on a restricted gene panel and a matched scRNA-seq reference (Fig. 1), BRIDGE proceeds in three stages. First, the reference is lightly denoised to reduce dropout and stabilize downstream alignment and prediction. Second, biologically meaningful anchor pairs linking spatial and reference cells are identified, and a global nonnegative calibration matrix is learned to linearly align expression across shared genes. Third, using the calibrated reference manifold, BRIDGE imputes unmeasured genes through multi-scale k-nearest neighbor regression, combining predictions across multiple neighborhood sizes to obtain a robust and interpretable transcriptome for each spatial cell. This three-stage design maintains biological structure during cross-modal calibration, mitigates distortions common to latent-space alignment, and produces interpretable calibration weights, enabling downstream analyses such as spatial program discovery and fine-grained subtype characterization.

Conceptually, anchor-guided calibration in BRIDGE differs fundamentally from latent-space alignment approaches. Latent-space methods typically project reference and query data into a shared low-dimensional embedding space, where alignment is achieved implicitly by optimizing distances, batch-mixing objectives, or reconstruction losses. While effective for certain applications, such transformations obscure gene-level correspondences and make it difficult to trace how individual genes are adjusted during alignment.

In contrast, BRIDGE performs calibration directly in the original gene-expression space using anchor pairs as sparse but informative cross-modality correspondences.

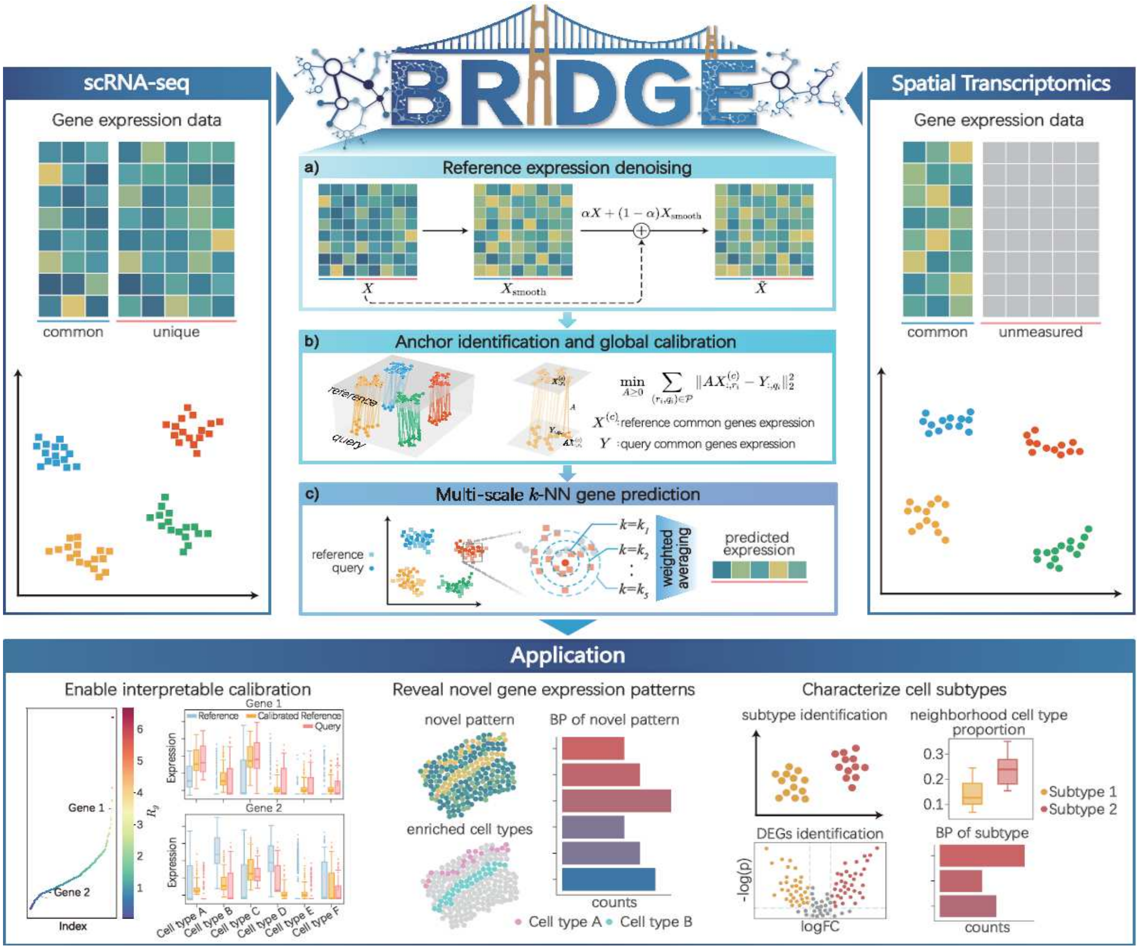

Figure 1: Overview of the BRIDGE framework for transcriptome-scale completion of imaging-based spatial transcriptomics. BRIDGE expands panel-limited spatial transcriptomics by leveraging a matched scRNA-seq reference through a structure-preserving, three-stage workflow. The process begins with the gene-expression matrices from a spatial query dataset and a scRNA-seq reference, which serve as the inputs for the subsequent stages. (a) The scRNA-seq reference is lightly denoised to reduce dropout and stabilize downstream calibration and prediction. (b) Biologically meaningful anchor pairs between reference and spatial cells are identified, and a global, nonnegative gene-gene calibration matrix is learned to linearly align shared-gene expression directly in gene-expression space, preserving intrinsic biological geometry while avoiding under- or over-alignment. (c) Using the calibrated reference manifold, unmeasured genes are predicted for each spatial cell via multi-scale k-nearest neighbor aggregation across multiple neighborhood sizes, yielding robust and interpretable transcriptome-scale predictions. Together, these steps decouple global cross-modal calibration from local neighborhood-based prediction, enabling accurate and biologically interpretable spatial gene completion and downstream analyses such as spatial program discovery and fine-grained subtype characterization.

These anchors are used to estimate a global, gene-to-gene calibration matrix that linearly transforms reference expression profiles toward the spatial domain on shared genes, serving as sparse constraints for learning a global calibration rather than mediating direct expression transfer between individual cell pairs. This design preserves the original data dimensionality, yields an explicit and nonnegative mapping that can be directly inspected, and enables transparent interpretation of gene-wise adjustment patterns. By avoiding reliance on latent representations, BRIDGE maintains interpretable gene-level relationships while still achieving robust alignment between reference and spatial datasets.

2.1.1 Reference expression denoising

Dropout and technical noise in the scRNA-seq reference can obscure true transcriptional signals and affect operations that rely on gene-wise expression levels, including estimation of the global calibration matrix and downstream k-NN prediction. To mitigate these effects while preserving the intrinsic structure of the reference manifold, BRIDGE applies MAGIC [58] to smooth dropout-affected expression through graph-based local averaging in gene-expression space. MAGIC is used here in a conservative manner to stabilize reference expression under sparsity, rather than to reconstruct fine-scale gene-gene correlations or impose strong assumptions on expression structure. Specifically, we use a minimal diffusion setting (diffusion time $t=1$) to limit smoothing to immediate local neighborhoods and avoid over-smoothing. This results in a more coherent and biologically consistent representation of the reference transcriptome that supports robust calibration and prediction.

Let the preprocessed reference expression matrix be $X \in \mathbb{R}^{(G_c+G_u)\times N_r}$, and let X_{smooth} denote the MAGIC-smoothed matrix. Here, N_r is the number of reference cells, G_c is the set of genes shared with the spatial dataset, and G_u denotes reference-unique genes. To balance fidelity to the original measurements with the benefits of smoothing, BRIDGE forms a weighted combination

$$\tilde{X} = \alpha X + (1-\alpha) X_{\text{smooth}} \tag{2.1}$$

with $\alpha = 0.5$. This value serves as a balanced default that moderates the influence of imputed signals and is not critical to model performance, as demonstrated by sensitivity analyses across a range of α values (Supplementary materials [76]). The resulting representation reduces random dropout while preserving cell-type-resolving variation. For notational simplicity, we use X to denote $\tilde{X}$ in the subsequent sections.

Although MAGIC is adopted as the default denoising strategy for its simplicity and computational efficiency, reference denoising in BRIDGE is not method-specific. In principle, alternative denoising approaches such as ALRA [30] or SAVER [25] can be readily incorporated without altering the global calibration or multi-scale prediction mechanisms.

2.1.2 Anchor identification and global calibration

To relate spatial cells to transcriptionally similar reference cells, BRIDGE first identifies cross-dataset anchors between the scRNA-seq reference and the spatial query. Anchor detection is performed using Seurat's `FindIntegrationAnchors` function [23] with default parameters. Because MAGIC operates on preprocessed expression data while Seurat relies on raw counts for anchor discovery, we provide Seurat with the original raw count matrices. This preserves compatibility with Seurat's integration model and ensures that anchor identification is driven by native expression signals, whereas the denoised reference representation is reserved for calibration and prediction.

Seurat returns a set of anchor pairs $\mathcal{P}=\{(r_i,q_i)\}_{i=1}^{N_a}$, where (r_i,q_i) indexes the i-th matched reference-query pair and N_a is the total number of anchors. These anchors capture biologically meaningful correspondences and provide sparse, local constraints describing how shared-gene expression should relate across modalities.

Although anchors encode reliable cross-dataset matches, they cover only a fraction of all cell pairs and do not provide a global mapping between technologies. Relying solely on anchors for transfer can amplify noise in individual matches and fails to provide a gene-level description of how expression scales or recombines across platforms. BRIDGE addresses this limitation by using the anchor set $\mathcal{P}$ as supervision to learn a global gene-gene calibration matrix that linearly aligns the reference and query datasets on their shared genes.

The use of a single global linear calibration matrix is motivated by the observation that a substantial portion of the systematic discrepancies between imaging-based spatial transcriptomics and scRNA-seq can be attributed to technology-level effects, which tend to act consistently across cells. Under this assumption, a linear transformation provides an identifiable and interpretable mechanism for correcting cross-modality bias on shared genes, while avoiding overfitting to cell-specific noise. Importantly, the calibration matrix is not intended to model fine-grained biological heterogeneity across cells, but rather to remove systematic technology-driven variation so that reference and spatial expression profiles become comparable in the original gene-expression space.

Let $X^{(c)}\in\mathbb{R}^{G_c\times N_r}$ denote the reference expression matrix restricted to common genes, and let $Y\in\mathbb{R}^{G_c\times N_q}$ denote the corresponding query expression matrix. BRIDGE learns a nonnegative calibration matrix $A\in\mathbb{R}^{G_c\times G_c}$ such that transformed reference profiles $AX^{(c)}$ align with query profiles on the anchor pairs. The optimization objective is

$$\begin{aligned}&\min_{A}\sum_{(r_i,q_i)\in\mathcal{P}}\left\|AX^{(c)}_{:,r_i}-Y_{:,q_i}\right\|_2^2\\&\text{subject to}\quad A\geq 0.\end{aligned}\tag{2.2}$$

Here, A acts as a global calibration operator whose entries quantify how expression of one gene in the reference is linearly reweighted by others to match the query. The elementwise nonnegativity constraint prevents implausible negative coefficients and yields biologically interpretable additive transformations.

For compactness, define binary matrices $D_1\in\{0,1\}^{N_r\times N_a}$ and $D_2\in\{0,1\}^{N_q\times N_a}$, whose i-th columns encode the locations of r_i and q_i respectively. The objective then becomes a Frobenius-norm least squares problem

$$\begin{aligned}&\min_{A}\left\|AX^{(c)}D_1-YD_2\right\|_F^2\\&\text{subject to}\quad A\geq 0.\end{aligned}\tag{2.3}$$

We optimize Eq. (2.3) using a projected first-order method. For

$$f(A)=\left\|AX^{(c)}D_1-YD_2\right\|_F^2,$$

each update takes the form

$$A^{(k+1)}=\left[A^{(k)}-\eta_k\nabla f(A^{(k)})\right]_+, \tag{2.4}$$

where $[\cdot]_+$ denotes elementwise projection onto the nonnegative orthant. We adopt Adam with a base learning rate of 10^{-3} for step-size adaptation, and apply the projection after each update. Optimization terminates when the relative change

$$\frac{\|A^{(k+1)}-A^{(k)}\|_F}{\max\left(1,\|A^{(k)}\|_F\right)}<10^{-5}$$

is satisfied or when 2,000 iterations are reached.

Upon convergence, we obtain the calibration matrix A. Applying A to the common-gene reference matrix yields the calibrated representation

$$\hat{X}^{(c)}=AX^{(c)}, \tag{2.5}$$

which generalizes the anchor-derived constraints across all reference cells. This globally calibrated reference manifold forms the basis for BRIDGE's subsequent neighborhood-based imputation of unmeasured genes.

2.1.3 Multi-scale *k*-NN gene prediction

After global calibration removes technology-level bias, cell-level biological variation is recovered through neighborhood-based prediction. The multi-scale *k*-NN aggregation operates on the calibrated expression manifold and leverages local similarity structure to capture fine-grained heterogeneity that cannot be represented by a global linear transformation alone.

Given the calibrated reference matrix $\hat{X}^{(c)}$, BRIDGE predicts unmeasured gene expression in the spatial dataset through neighborhood-based regression in the common-gene space. A single fixed choice of neighborhood size k corresponds to a fixed bias-variance tradeoff. Small k preserves fine-grained local structure but can exhibit high variance due to noise, whereas large k reduces variance at the cost of increased bias by over-smoothing biological heterogeneity. Rather than committing to a single operating point on this tradeoff, BRIDGE adopts a multi-scale *k*-NN strategy that aggregates predictions across multiple neighborhood sizes, thereby implicitly balancing bias and variance in a data-adaptive manner and reducing sensitivity to the choice of k.

Specifically, BRIDGE uses a set of neighborhood sizes $\mathcal{K}=\{10,20,30,40,50\}$, producing a collection of base regressors that reflect different levels of local smoothness. For each $k\in\mathcal{K}$, BRIDGE computes query-reference distances in the common-gene space and performs similarity-weighted *k*-NN regression.

For each query cell j and reference cell i, the Euclidean distance is

$$d(j,i)=\sqrt{\sum_{l=1}^{G_c}\big(Y[l,j]-\hat{X}^{(c)}[l,i]\big)^2}, \tag{2.6}$$

where $Y[l,j]$ and $\hat{X}^{(c)}[l,i]$ denote the expression levels of gene l in the query and calibrated reference, respectively. For scale k, BRIDGE identifies the k nearest reference neighbors of cell j, denoted $\mathcal{N}_k(j)$, and constructs a sparse similarity matrix $W_k\in\mathbb{R}^{N_q\times N_r}$ with nonzero entries

$$W_k[j,i]=\begin{cases}\dfrac{1}{d(j,i)}, & \text{if} \quad i\in\mathcal{N}_k(j),\\ 0, & \text{otherwise}.\end{cases} \tag{2.7}$$

The corresponding base prediction $\hat{Y}_{u,k}\in\mathbb{R}^{G_u\times N_q}$ for unmeasured genes is obtained by similarity-weighted averaging

$$\hat{Y}_{u,k}[l',j]=\frac{\sum_{i'=1}^{N_r}W_k[j,i']X^{(u)}[l',i']}{\sum_{i'=1}^{N_r}W_k[j,i']}, \tag{2.8}$$

where $X^{(u)}$ is the reference-unique gene expression matrix.

To combine predictions across scales, BRIDGE assigns each k a cell-specific reliability weight. For query cell j, the squared Pearson correlation between the predicted and observed common-gene expression provides a measure of reconstruction fidelity

$$\omega_k[j]=\mathrm{cor}^2\big(\hat{Y}_{c,k}[:,j],Y[:,j]\big),$$

where $\hat{Y}_{c,k}$ denotes the base prediction for the common genes at scale k. Higher $\omega_k[j]$ indicates that the neighborhood size k better reflects the transcriptomic structure around cell j. The final prediction integrates the multi-scale estimates using these weights

$$\hat{Y}_{u,\mathrm{final}}[l',j]=\frac{\sum_{k\in\mathcal{K}}\omega_k[j]\hat{Y}_{u,k}[l',j]}{\sum_{k\in\mathcal{K}}\omega_k[j]}. \tag{2.9}$$

By adaptively aggregating predictions across neighborhood scales, BRIDGE achieves robust and accurate imputation of unmeasured genes while avoiding dependence on an arbitrarily chosen neighborhood size. This multi-scale formulation preserves fine-grained structure where supported by the data while maintaining stability in sparser regions of the transcriptome.

2.2 Benchmarking and evaluation metrics

We benchmark BRIDGE against five state-of-the-art methods for spatial gene expression imputation: stPlus [11], SpaGE [2], Seurat [23], gimVI [33], and Tangram [5]. All methods are run with their default hyperparameters, and data preprocessing (including normalization and scaling) follows the procedures implemented in each method's official code. Because gimVI and Tangram output expression values on the raw count scale, whereas the other methods produce library size-normalized and log-transformed values, we rescale the predictions of gimVI and Tangram using the true median library size and apply a `log1p` transformation to ensure comparability across methods.

Performance is evaluated on spatially measured genes through fivefold cross-validation. The common genes shared between the spatial and scRNA-seq datasets are partitioned into five disjoint subsets. In each fold, one subset is held out for evaluation, and the remaining subsets are used for training the imputation model. This process is repeated across all folds such that every gene is predicted exactly once.

We quantify imputation accuracy using four complementary metrics computed at both the gene and cell levels: Pearson correlation coefficient (PCC), structural similarity index measure (SSIM), root mean square error (RMSE), and Jensen-Shannon divergence (JSD). Higher PCC and SSIM indicate stronger linear and structural agreement between measured and predicted expression, while lower RMSE and JSD reflect smaller magnitude and distributional discrepancies.

To summarize overall performance, we compute an aggregated accuracy score (AS) defined as the mean rank of each method across the four metrics

$$\mathrm{AS}=\frac{1}{4}\left(\mathrm{RANK}_{\mathrm{PCC}}+\mathrm{RANK}_{\mathrm{SSIM}}+\mathrm{RANK}_{\mathrm{RMSE}}+\mathrm{RANK}_{\mathrm{JSD}}\right),$$

where $\mathrm{RANK}_{(\cdot)}$ denotes the ranking position of each method under the respective metric. A larger AS corresponds to better overall performance.

Beyond global summary metrics, we also compute an accuracy ratio (AR) to compare BRIDGE with each competing method at the level of individual genes or cells. For any metric m, the AR is defined as

$$\mathrm{AR}(m)=\frac{|\{i: m_i(\mathrm{BRIDGE})>m_i(\mathrm{comp})\}|}{|\{i: m_i(\mathrm{BRIDGE})<m_i(\mathrm{comp})\}|},$$

where i indexes units (genes or cells) and $m_i(\cdot)$ is the metric value for that unit. For metrics minimized by optimal performance (e.g. RMSE and JSD), the inequalities are inverted equivalently by taking reciprocals. An $\mathrm{AR}>1$ indicates that BRIDGE outperforms the comparator on a larger proportion of units. Statistical significance is assessed using a paired Wilcoxon signed-rank test across genes or cells.

In addition, we evaluate the performance of different models in terms of alignment quality and geometric manifold preservation. For alignment, we compute k-nearest neighbor batch effect test (kBET) [7] and graph connectivity [34], which assess batch mixing in the embedding and the extent to which biologically similar cells remain connected after alignment, respectively. For geometric manifold preservation, we use k-NN preservation, trustworthiness, and continuity [61], which quantify the overlap of local neighborhoods and the fidelity of the embedding in retaining true neighbors while avoiding spurious ones. Higher values of these metrics indicate better performance in alignment and preservation of local structure. These metrics together provide a comprehensive evaluation of both dataset integration and geometric structure preservation in the learned embeddings.

2.3 Calibration interpretability analysis

The calibration matrix $A\in\mathbb{R}^{G_c\times G_c}$ learned by BRIDGE serves not only as the global operator aligning reference and query expression on shared genes, but also as an interpretable representation of how gene-gene relations differ between modalities. Each row of A corresponds to a target gene whose expression is calibrated, and each column captures the contribution of a source gene in forming its aligned expression profile. The nonnegativity constraint $A\geq 0$ ensures additive and biologically plausible transformations, avoiding negative coefficients that would imply implausible inhibitory effects at the level of cross-technology calibration.

To summarize the magnitude of calibration applied to each gene, we compute a row-wise aggregation index

$$R_g=\sum_j A_{g,j}, \tag{2.10}$$

which reflects the total scaling and redistribution required to align gene g between the reference and spatial datasets. Empirically, larger R_g values correspond to stronger upscaling adjustments needed to match the query distribution, whereas smaller values indicate milder calibration, often consistent with downscaling or minimal cross-modal discrepancy.

We assessed calibration interpretability using the MERFISH mouse primary motor cortex and human heart datasets, focusing on the first cross-validation fold as a representative run. In each dataset, BRIDGE was trained to estimate A using anchors derived from shared genes, after which we visualized the distribution of R_g across genes. The resulting profiles revealed substantial gene-specific heterogeneity in calibration magnitude, reflecting differences in how individual genes shift across technologies and highlighting the interpretability afforded by BRIDGE's explicit linear calibration model.

2.4 Spatial gene-expression pattern analysis of MERFISH mouse primary motor cortex (MOp) data

We analyzed measured and BRIDGE-predicted expression profiles to characterize spatial gene-expression patterns in the MERFISH mouse primary motor cortex, following established approaches [42, 64]. From the predicted expression matrix, we selected the top 5,000 highly variable genes (HVGs) for downstream analysis.

We first constructed reference spatial patterns using the measured genes. For each predicted gene, we quantified its spatial similarity to these reference patterns and clustered genes based on these similarity profiles, yielding pattern groups that jointly capture measured and predicted spatial structures. Representative predicted genes from each group were visualized to examine spatial coherence. To assess structural consistency, we compared the predicted spatial maps with in situ hybridization (ISH) and Expression images from the Allen Brain Atlas [28], and evaluated co-localization with annotated cell types.

Predicted genes that did not match any reference pattern were further analyzed through unsupervised clustering to identify additional spatial pattern groups. For each newly identified group, we repeated spatial visualization, Allen Brain Atlas comparison, and cell-type co-localization analysis. Lastly, we performed gene ontology (GO) enrichment using the `clusterProfiler` R package [69] on the gene sets in each group to contextualize their putative biological functions.

2.5 Cell subtype analysis of Xenium human breast cancer data

To resolve within-type heterogeneity in the Xenium human breast cancer dataset, we first combined the measured and BRIDGE-predicted expression matrices to obtain whole-transcriptome profiles and rescaled these values to match the scale of the reference data. Expression for the target cell type was then extracted, and the top 3,000 HVGs were selected to enhance subtype resolution. Using these HVGs, we applied Leiden clustering with the `scanpy` [63] implementation, setting the resolution parameter to 0.1 to identify fine-grained substructures within the target population.

Differentially expressed genes (DEGs) for each subtype were identified using `scanpy`'s `rank_genes_groups` function with an adjusted p-value threshold of $p_{\text{adj}} < 0.01$. For Stromal cells, we required a log fold change (logFC) greater than 1.5, and for B cells a threshold of logFC greater than 3, ensuring that selected DEGs exhibited strong subtype-specific upregulation.

Functional characterization of each subtype was performed by GO enrichment analysis on the subtype-specific DEGs using the `clusterProfiler` R package. To evaluate spatial organization, we mapped the spatial coordinates of all cells and computed the composition of neighboring cell types within a $100\,\mu$m radius of each cell. Differences in neighborhood composition across subtypes were assessed using two-sample t-tests with multiple-testing correction.

These analyses jointly evaluated the molecular and spatial distinctions between subtypes, providing functional context for subtype-specific DEGs and supporting the accuracy of BRIDGE-generated transcriptome predictions. To harmonize annotations and treat proliferation as a continuous attribute rather than a distinct class, we merged the Xenium labels Invasive Tumor and Prolif Invasive Tumor into a single Invasive Tumor category.

2.6 Ablation and sensitivity analysis

We performed a set of ablation and sensitivity analyses to evaluate the robustness of BRIDGE with respect to anchor quality and model parameterization. Detailed quantitative results are provided in the Supplementary materials.

We first examined the sensitivity of BRIDGE to imperfect or noisy anchors by perturbing the anchor set identified by Seurat. Specifically, we randomly removed or injected a small fraction of anchor pairs and evaluated the impact on downstream prediction. Across all perturbation settings, BRIDGE maintained stable performance with only minor fluctuations observed across evaluation metrics. This stability reflects the fact that anchors are used as sparse constraints for learning a global calibration matrix, rather than as direct carriers of expression transfer.

We further assessed the sensitivity of BRIDGE to reference denoising and model parameters by varying the strength of MAGIC-based denoising and comparing it with alternative strategies, and a no-denoising baseline. Across these settings, the learned calibration matrices remained highly consistent and downstream prediction performance varied smoothly, indicating that BRIDGE is robust to reasonable choices of denoising strength and parameter settings.

Together, these analyses demonstrate that BRIDGE yields stable calibration and prediction results under variations in anchor quality and model parameterization.

2.7 Datasets

We benchmarked BRIDGE across seven spatial transcriptomics datasets spanning three technologies (MERFISH, Xenium, and CosMx), multiple species, and diverse tissue contexts. Each spatial dataset was paired with a matched scRNA-seq reference generated from the same or a closely related tissue. A summary of all spatial datasets and their corresponding references is provided in Table 1.

The CosMx mouse brain dataset was obtained from NanoString (`https://nanostring.com/products/cosmx-spatial-molecular-imager/ffpe-dataset/cosmx-smi-mouse-brain-ffpe-dataset/`), and its matched reference is described in [67]. The MERFISH mouse POA dataset was downloaded from Dryad (`https://datadryad.org/stash/`

Table 1: Summary of the benchmarking datasets used in this study.

Data pair		Spatial data			scRNA-seq data		
Species	Tissue	# of cells	# of genes	Technology	# of cells	# of genes	Technology
Mouse	brain	48,180	927	CosMx	73,347	41,555	SMART-Seq v4
Mouse	POA	23,068	154	MERFISH	31,299	20,339	10x Chromium
Human	heart	72,962	238	MERFISH	22,804	22,678	10x Chromium v2
Human	healthy kidney	97,511	362	Xenium	33,690	17,816	scFFPE-seq
Human	PRCC	56,504	339	Xenium	11,949	21,613	10x Chromium v3
Mouse	MOp	4,408	251	MERFISH	26,714	25,683	10x Chromium v3
Human	breast cancer	159,226	306	Xenium	27,460	16,938	scFFPE-seq

Note: POA, hypothalamic preoptic region; MOp, primary motor cortex; PRCC, papillary renal cell carcinoma.

`dataset/doi:10.5061/dryad.8t8s248`), with its scRNA-seq reference available under GEO accession GSE113576 [43]. The MERFISH human heart dataset and its matched reference were obtained from [18]. Human healthy kidney and PRCC Xenium datasets were downloaded from `https://www.10xgenomics.com/cn/datasets/human-kidney-preview-data-xenium-human-multi-tissue-and-cancer-panel-1-standard`. The healthy kidney reference dataset is available at `https://www.10xgenomics.com/cn/datasets/320k_scFFPE_16-plex_GEM-X_FLEX`, and the PRCC reference can be accessed under GEO accession GSE152938 [52]. The MERFISH mouse MOp dataset was downloaded from `https://doi.org/10.35077/g.21` [72], and its matched scRNA-seq reference is available from the NeMO archive (`https://data.nemoarchive.org/biccn/lab/zeng/transcriptome/scell/10x_v3/mouse/processed/analysis/10X_cells_v3_AIBS/`) [66]. The Xenium human breast cancer dataset and its reference dataset are described in [26]. Detailed preprocessing procedures for each dataset are described in the Supplementary materials.

3 Results

3.1 BRIDGE achieves competitive and robust performance across diverse datasets

To evaluate the predictive accuracy and generalizability of BRIDGE, we assembled seven spatial transcriptomics datasets covering three technologies, multiple species, and diverse tissue contexts. We first benchmarked BRIDGE on two representative datasets, CosMx mouse brain and MERFISH human heart, using fivefold cross-validation and compared its performance against five state-of-the-art methods (stPlus [11], SpaGE [2], Seurat [23], gimVI [33], and Tangram [5]). These analyses allowed us to assess model behavior at both the gene- and cell-level and to examine its consistency across distinct biological settings.

For the CosMx mouse brain dataset, fivefold cross-validation was performed on 927 shared genes between reference and query. At the gene-level, BRIDGE matched SpaGE and outperformed the remaining methods across all evaluation metrics (Fig. 2(A), Supplementary Figs. S1 and S2). At the cell-level, BRIDGE consistently achieved the highest accuracy across multiple metrics (Supplementary Figs. S1 and S3). Combined gene- and cell-level Accuracy Scores confirmed its overall superiority (Fig. 2(B)). Spatial visualizations for genes such as *Pcp4*, *Kalrn*, *Rasgrf2*, and *Slc32a1* further illustrated BRIDGE's accurate reconstruction of regional expression patterns, with *Pcp4* in the hippocampal region serving as a representative example (Fig. 2(C) and Supplementary Fig. S4).

On the MERFISH human heart dataset, BRIDGE again demonstrated clear advantages. At the gene-level, BRIDGE yielded higher PCC and SSIM and lower RMSE and JSD compared with all baseline methods (Supplementary Figs. S5 and S6). Similar improvements were observed at the cell-level (Supplementary Figs. S5 and S7). Accuracy ratios and Wilcoxon signed-rank tests further indicated significant improvements in PCC,

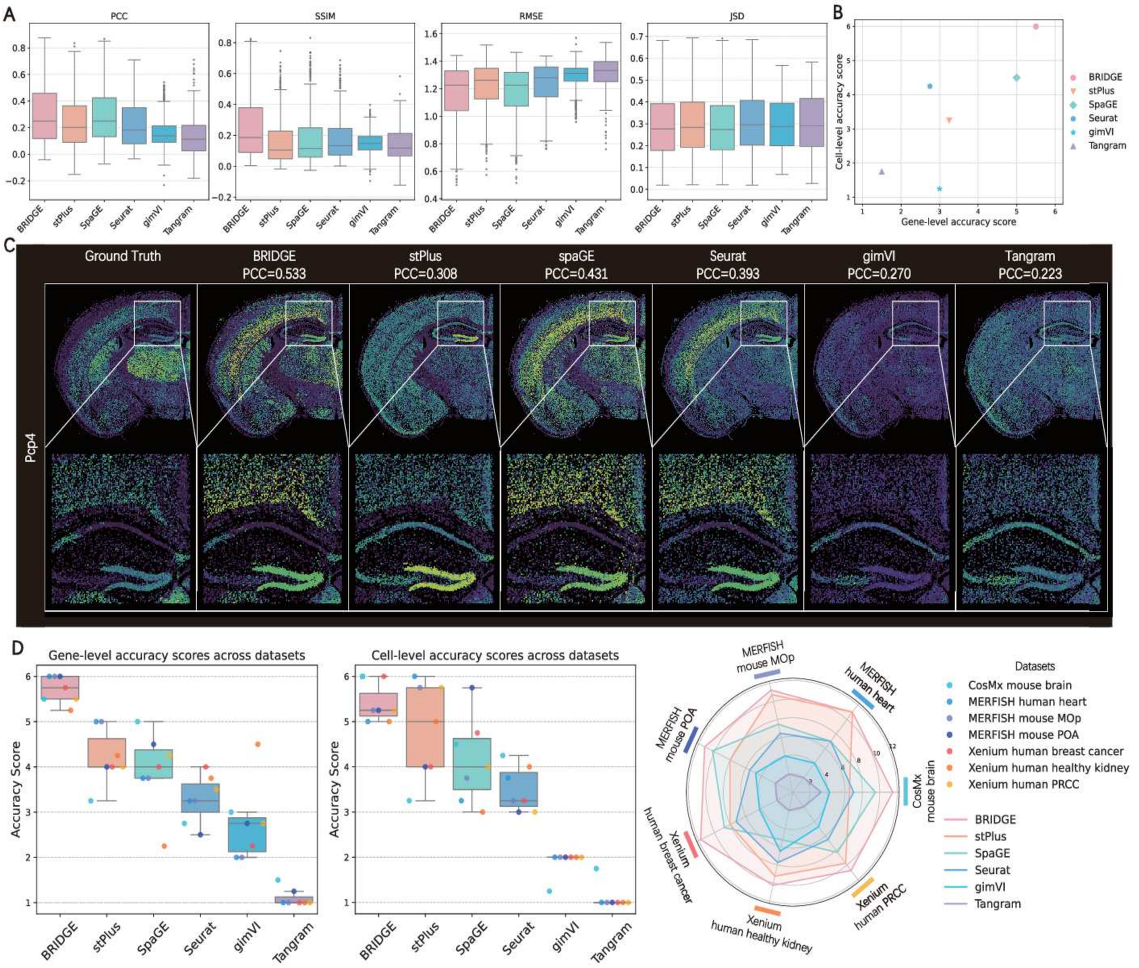

Figure 2: Performance comparison between BRIDGE and five benchmarked methods via fivefold cross-validation. (A) Gene-level performance across four metrics for the CosMx mouse brain dataset. (B) Gene- and cell-level accuracy scores (AS) for the CosMx dataset. Higher values indicate better performance. (C) Spatial expression of measured and predicted *Pcp4* in the CosMx dataset across methods. (D) Summary of BRIDGE and comparator performance across all seven datasets, including AS boxplots at the gene- and cell-level and an aggregate radar plot. Each radar axis represents a dataset, with values corresponding to the sum of gene- and cell-level AS.

SSIM, and RMSE; although JSD differences were not statistically significant, BRIDGE still achieved consistently higher AR values. Visualization of spatial expression patterns for *HCN4*, *FNDC1*, *BMP2*, and *COL9A2* reinforced BRIDGE's strong performance (Supplementary Fig. S8).

To assess broader generalization, we extended benchmarking to the remaining datasets (Supplementary Figs. S9-S28). Across all datasets, BRIDGE delivered the highest gene-level accuracy in most settings (Fig. 2(D)), reflecting precise per-gene reconstruction. At the cell-level, BRIDGE remained highly competitive, frequently ranking among the top-performing methods across evaluation metrics and datasets (Fig. 2(D)). A global comparison summarized in a radar plot further highlighted BRIDGE's strong and stable behavior across heterogeneous technologies and tissues. In contrast, several competing methods, such as stPlus, showed pronounced dataset-dependent variability, performing well on some datasets but noticeably worse on others.

Notably, the datasets included in this benchmark exhibit substantial heterogeneity in data quality, with pronounced variation in cell-level sparsity and gene-level detection rates across both reference and spatial measurements (Supplementary Fig. S29). These metrics capture heterogeneity associated with dropout and incomplete gene detection that are commonly encountered in imaging-based spatial transcriptomics. Despite this variability, BRIDGE consistently achieves strong predictive performance across datasets, indicating robustness to heterogeneous sparsity and data incompleteness in practice.

Together, these comprehensive evaluations demonstrate that BRIDGE achieves consistently strong predictive accuracy at both the gene- and cell-level across a wide range of spatial transcriptomics platforms and biological contexts. Its robustness, stability, and cross-dataset generalizability establish BRIDGE as a reliable and effective framework for transcriptome-scale completion in panel-limited spatial assays.

3.2 BRIDGE enables interpretable calibration and structure-preserving integration

Interpretability is essential for models that transfer information across modalities, yet many existing approaches rely on latent representations whose alignment cannot be traced back to gene-level effects [35]. To examine the interpretability of BRIDGE, we analyzed its learned calibration matrix A on MERFISH mouse primary motor cortex and human heart datasets.

On the MOp dataset, the row-sum index $R_g = \sum_j A_{g,j}$ revealed substantial gene-to-gene variability in calibration magnitude (Fig. 3(A)). Four representative genes (*Sulf2*, *Pcdh8*, *Unc5d*, *Lyzl4*) exhibited clear discrepancies between the original reference and query distributions, yet the calibrated reference aligned closely with the query following BRIDGE transformation (Fig. 3(B)). Larger R_g values corresponded to stronger up-scaling required to match the query distribution, whereas smaller values reflected down-scaling. Quantitatively, the per-gene mean expression shift (calibrated minus original reference) showed a strong Spearman correlation with R_g ($r = 0.752$, Fig. 3(C)), supporting R_g as a reliable gene-level indicator of calibration direction and intensity.

To assess whether calibration preserves biological manifold structure, we compared low-dimensional embeddings before and after calibration, alongside four latent-space alignment methods (stPlus, SpaGE, Seurat, and gimVI) (Fig. 3(D)). Tangram was excluded due to its mapping-rather-than-integration design. BRIDGE produced an integrated embedding in which reference and query cells aligned while retaining the intrinsic geometry of the MOp manifold. In contrast, SpaGE and Seurat distorted rare populations, and gimVI collapsed multiple excitatory neuron subtypes into a compressed latent trajectory, losing biologically meaningful distinctions.

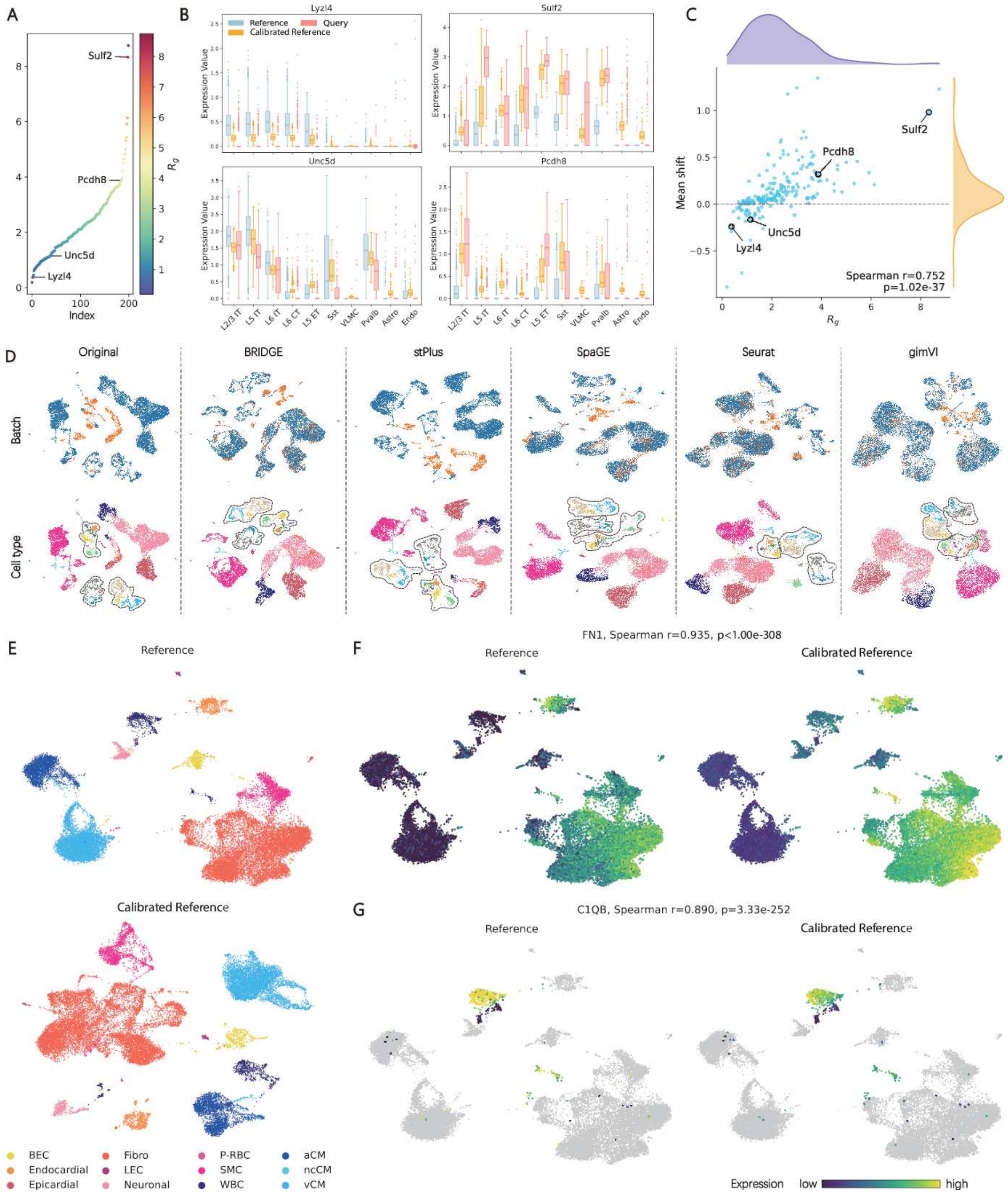

Figure 3: Interpretable calibration in BRIDGE, illustrated on mouse primary motor cortex and human heart datasets. (A) Sorted distribution of the row-sum index R_g on the MERFISH mouse MOp dataset, highlighting four representative genes. (B) Gene expression distributions across major cell types for the reference, BRIDGE-calibrated reference, and query datasets. (C) Relationship between the per-gene mean expression shift and R_g. (D) UMAP visualizations of common-gene expression from the reference and query datasets before and after BRIDGE calibration, compared with embeddings from four alignment-based methods. (E) UMAP of the human heart reference before and after calibration. (F) *FN1* heatmaps on the reference UMAP before and after calibration. (G) *C1QB* expression within the WBC lineage before and after calibration.

Analogous interpretability was observed in the human heart dataset. Four representative genes (*FN1*, *SPON2*, *C1QB*, *HHIP*) showed strong agreement between gene-wise mean expression shift and R_g (Supplementary Fig. S30). UMAPs generated from reference and calibrated expression preserved global structure (Fig. 3(E)). Heatmaps of *FN1* on a fixed reference UMAP exhibited high concordance before and after calibration ($r=0.935$, Fig. 3(F)), and *C1QB* expression within the WBC lineage similarly retained relative expression intensities ($r=0.890$, Fig. 3(G)).

To complement these qualitative assessments, we further performed quantitative evaluation using five complementary metrics. Manifold geometry preservation was assessed using k-NN preservation, trustworthiness, and continuity, which quantify the consistency of local and global neighborhood relationships before and after calibration. In addition, cross-dataset alignment was evaluated using kBET and graph connectivity, which measure the extent to which reference and query cells are coherently aligned in the calibrated space. Across both the mouse MOp and human heart datasets, BRIDGE consistently achieved strong performance across all five metrics, supporting its ability to preserve intrinsic manifold geometry while maintaining accurate alignment between reference and spatial datasets (Supplementary Fig. S31).

In summary, analyses on mouse cortex and human heart show that BRIDGE's calibration matrix A provides a transparent gene-level readout. The row-sum index R_g captures both the magnitude and direction of calibration and exhibits strong correlations with gene-wise shifts in mean expression. BRIDGE also preserves global manifold geometry, as supported by both qualitative visualization and quantitative evaluation using complementary geometric and correspondence-based metrics. These characteristics are consistent across tissues and species, demonstrating that BRIDGE supports interpretable and structure-preserving integration. In practical applications, A and R_g serve as informative diagnostics that reveal gene-level discrepancies between modalities, identify potential panel imbalances, and guide downstream analyses. This combined behavior illustrates that BRIDGE unifies predictive accuracy with biological interpretability.

3.3 BRIDGE reveals novel gene expression patterns in the mouse primary motor cortex

Identifying spatial gene expression patterns is essential for understanding tissue organization and underlying biological processes [41,66]. In the brain, spatial gene signatures inform regulatory programs and neuronal function [74], yet imaging-based spatial transcriptomics measures only a small subset of genes, limiting comprehensive pattern discovery. To overcome this limitation, we applied BRIDGE to the MERFISH MOp dataset, which contains well-defined cortical layers that provide a strong anatomical scaffold. BRIDGE predicted the expression of 25,432 unmeasured genes using 251 shared genes between the reference and query datasets, enabling near-transcriptome-scale pattern discovery.

We first examined the spatial organization of BRIDGE's predictions. Many predicted genes exhibited clear laminar architecture consistent with in situ hybridization and Expression images from the Allen Brain Atlas [28] (Supplementary Fig. S32). Several well-characterized markers were accurately reconstructed. For example, *Ctgf* and *Tle4*, markers of layers L6b and L6a [45], displayed layer-specific enrichment in both predicted and reference images. *Deptor*, associated with L5/6 IT neurons [21], showed strong deep-layer localization. Genes enriched in L2/3 IT neurons, including *Wfs1* and *Cpne6* [49], were correctly localized to superficial layers. In addition, *Nos1ap*, a gene involved in cortical development [8], displayed a spatial pattern consistent with its known biology. These consistent observations indicate that BRIDGE reconstructs biologically meaningful spatial landscapes far beyond the measured panel.

To systematically characterize spatial organization, we applied a graph-based co-expression framework [42, 64] to predicted profiles. Canonical spatial patterns were first derived from measured genes. We then compared these references with the top 5,000 highly variable predicted genes, identifying four shared spatial patterns. Averaged spatial profiles of measured and predicted genes showed strong agreement (Fig. 4(A), first and second rows). Representative predicted genes within each pattern matched ISH and Expression images from the Allen Brain Atlas (Fig. 4(A), third to fifth rows). The four shared patterns also showed distinct co-localization with canonical cell types, including three enriched in excitatory neurons and one associated with oligodendrocytes (Fig. 4(A), bottom row). These results demonstrate that BRIDGE accurately recovers established spatial gene-expression structures.

Beyond shared patterns, BRIDGE uncovered three spatial patterns not present in the measured genes (Fig. 4(B)). Representative genes for each pattern were validated using Allen Brain Atlas images, and biological relevance was assessed through spatial co-localization and functional enrichment (Figs. 4(B), 4(C) and Supplementary Fig. S33). Novel Pattern 1 was enriched in astrocytes (Astro), endothelial cells (Endo), perivascular macrophages (PVM), and vascular leptomeningeal cells (VLMC). Enriched GO terms included endothelial and epithelial cell migration, vasculogenesis, actin filament organization, and extracellular matrix secretion, consistent with roles of vascular-associated glia and Stromal cells in vascular development and tissue homeostasis [1, 17, 36, 44, 68, 70]. Novel Pattern 2 primarily co-localized with Astro and VLMC, which mediate vascular maintenance and support neural development. VLMC are known contributors to extracellular matrix organization, and astrocytes regulate neurogenesis and vascular function [44, 55, 60]. Correspondingly, enriched functions included neural precursor proliferation, neurogenesis, forebrain development, and adhesion. Novel Pattern 3 involved microglia (Micro), Endo, PVM, and pericytes (Peri), with functional enrichment related to antiviral defense and neuroinflammation. These findings align with documented roles of these cell types in immune modulation and vascular regulation [3, 16, 19, 20, 47, 54].

In summary, concordance with in situ images, cell-type co-localization, and functional enrichment demonstrates that BRIDGE not only recovers known spatial gene-expression patterns but also reveals biologically interpretable structures that extend beyond the scope of current imaging-based assays.

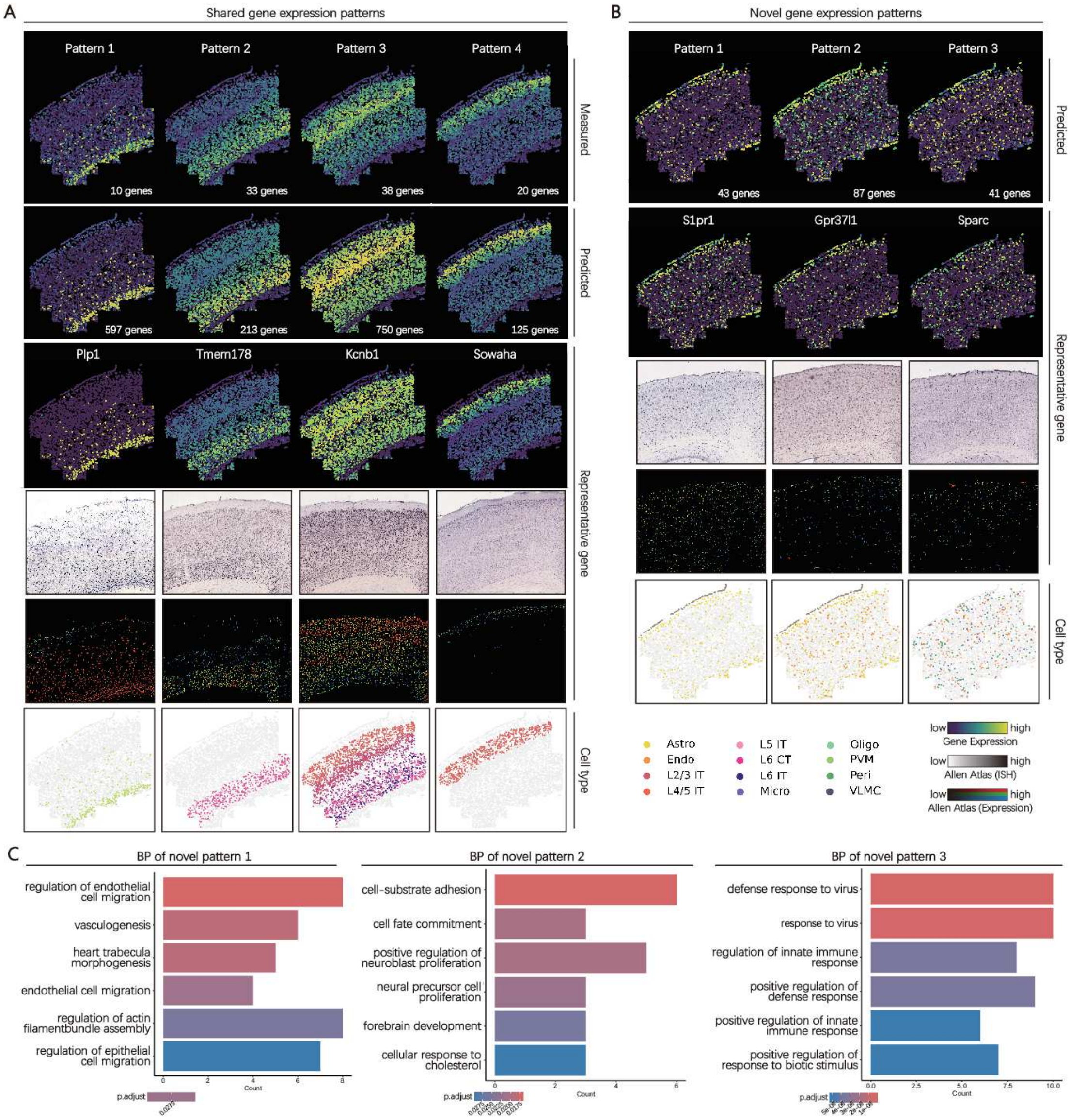

Figure 4: Identification and analysis of gene expression patterns in the MOp dataset. (A) Shared spatial patterns between measured and predicted genes. Top two rows show averaged measured and predicted patterns, respectively. Rows three to five show representative predicted genes and their ISH and expression images from the Allen Brain Atlas. The bottom row shows co-localizing cell types. (B) Three newly identified spatial patterns unique to predicted genes, with representative genes validated using the Allen Brain Atlas and corresponding cell-type co-localization. (C) GO enrichment analysis of genes in the newly identified patterns.

3.4 BRIDGE characterizes cellular subtypes in human breast cancer data

Characterizing cellular subtypes is fundamental for understanding tumor heterogeneity and progression [31]. Spatial transcriptomics preserves tissue context for such analyses

[14], but imaging-based assays measure only limited gene panels, constraining subtype resolution and obscuring subtle transcriptional differences. Applying BRIDGE to the Xenium human breast cancer dataset enabled transcriptome-scale reconstruction from 306 shared genes, yielding predictions for 16,632 unmeasured genes and supporting refined analyses of cellular diversity and spatial organization in the tumor microenvironment.

Using the combined matrix of measured and BRIDGE-predicted genes, we generated a UMAP embedding of all cells and observed clear preservation of major cell types (Fig. 5(A)). We next examined B cells to assess subtype diversity. Leiden clustering identified two transcriptionally distinct B-cell subtypes that separated clearly in UMAP space (Fig. 5(B)). Subtype 1 was broadly dispersed with local clusters, whereas subtype 2 formed compact aggregates across multiple regions (Fig. 5(C)). Twelve B-cell marker genes supported this split, including six measured (*TENT5C*, *MZB1*, *CD27*, *CD19*, *MS4A1*, *BANK1*) and six predicted (*XBP1*, *IRF4*, *CD38*, *PAX5*, *BLK*, *CD22*). Known functions of these genes further supported the distinction: *MS4A1* marks mature B cells [40], *CD27* marks memory B cells [59], *XBP1* regulates plasma-cell differentiation [46], and *CD22* modulates B-cell receptor signaling [57]. Marker expression patterns were consistent with the reference scRNA-seq dataset obtained from an adjacent tissue slice (Supplementary Figs. S34(A) and S34(B)).

Using full transcriptome profiles, we identified DEGs between the two B-cell subtypes and performed functional enrichment analysis. DEG expression corresponded closely with spatial distributions (Fig. 5(E) and Supplementary Fig. S34(D)). Subtype 1 was enriched for processes related to mitotic cell-cycle regulation and chromosome segregation (Fig. 5(F) and Supplementary Fig. S34(C)), resembling the c13_Bgc_DZ subtype described in recent pan-cancer analyses [65]. Subtype 2 was enriched for B-cell activation, receptor signaling, lymphocyte differentiation, and cytokine production (Fig. 5(G) and Supplementary Fig. S34(C)) [6, 38, 56]. Spatial neighborhood analysis showed that subtype 1 was preferentially surrounded by Stromal cells, consistent with a proliferative environment, whereas subtype 2 was enriched for T-cell neighbors and had fewer Stromal cells, consistent with its immune-related functions (Fig. 5(H), 5(I), Supplementary Figs. S34(E) and S34(F)).

Because Stromal cells appeared across neighborhoods of both B-cell subtypes, we investigated Stromal heterogeneity using transcriptome-wide profiles. Leiden clustering identified 11 transcriptionally distinct Stromal subtypes with clear separation in UMAP and distinct tissue localization patterns (Figs. 5(J), 5(K) and Supplementary Fig. S35). Subtype-specific DEGs and enriched biological processes characterized each subtype (Supplementary Figs. S36 and S37).

Stromal subtype 1 was enriched for extracellular-matrix programs, aligning with canonical stromal roles [27,37]. It showed broad spatial distribution and balanced neighborhoods lacking a dominant partner cell type (Supplementary Fig. S38). In contrast, subtypes 5 and 6 displayed particularly distinct biological and spatial signatures (Fig. 5(K)). Subtype 5 was enriched for cell-division programs and was predominantly neighbored by invasive tumor cells (Figs. 5(L), 5(M), Supplementary Figs. S37-S39), consistent with

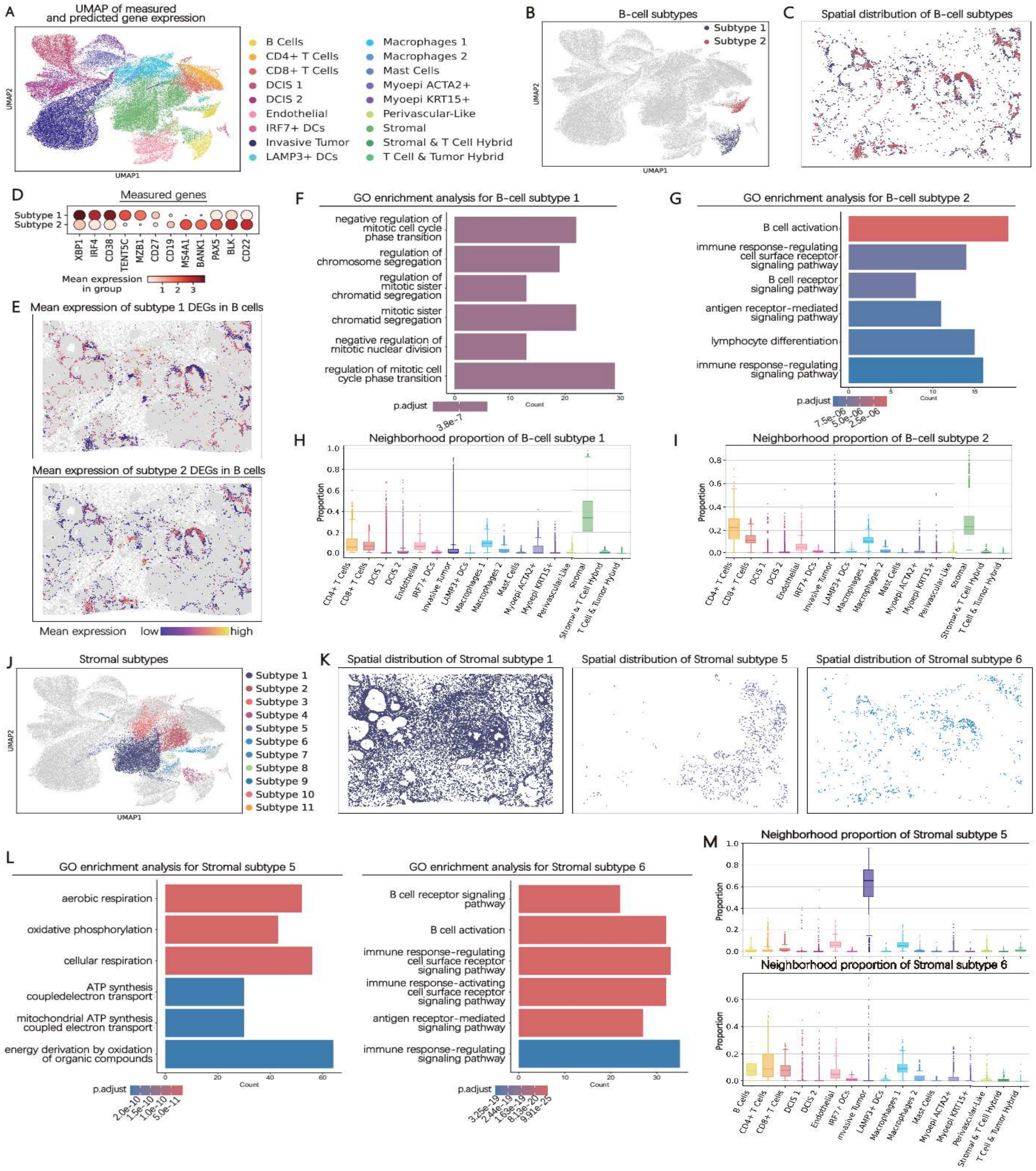

Figure 5: Identification and analysis of cellular subtypes and spatial organization in the Xenium human breast cancer dataset. (A) UMAP based on measured and predicted gene expression. (B) Two B-cell subtypes identified by Leiden clustering. (C) Spatial distribution of the two B-cell subtypes. (D) Dot plot of 12 B-cell marker genes, including six measured and six predicted. (E) Mean expression of DEGs for each B-cell subtype. (F, G) GO enrichment for B-cell subtype 1 and subtype 2, respectively. (H, I) Neighborhood compositions of B-cell subtype 1 and subtype 2. (J) UMAP of Stromal subtypes identified by BRIDGE. (K) Spatial distribution of Stromal subtypes 1, 5, and 6. (L) GO enrichment comparing Stromal subtypes 5 and 6. (M) Neighborhood compositions of Stromal subtypes 5 and 6.

stromal programs that support tumor proliferation [4, 37]. Subtype 6 exhibited strong enrichment for immune-related functions and preferentially neighbored B cells, T cells, and Macrophages (Figs. 5(L), 5(M), Supplementary Figs. S37-S39), in line with stromal-immune interactions that support antitumor responses [27, 37].

Together, BRIDGE enabled transcriptome-scale reconstruction in Xenium breast cancer data, revealing fine-grained cellular subtypes and heterogeneous stromal programs that are not fully captured by imaging-based panels. These analyses highlight BRIDGE's ability to refine cellular phenotypes and uncover spatial and functional organization within the tumor microenvironment.

4 Discussion

In this study, we introduced BRIDGE, an interpretable computational framework that extends imaging-based spatial transcriptomics from targeted panels to transcriptome-scale, cell-resolved maps by explicitly addressing the structural challenge of cross-modal alignment. Unlike methods that rely on latent-space matching, BRIDGE performs an anchor-guided global calibration directly in gene-expression space, reframing spatial gene prediction as a structure-preserving cross-modal calibration paradigm. This strategy yields an explicit, nonnegative calibration matrix that makes cross-modality alignment transparent, mitigates both under- and over-alignment, and preserves the intrinsic manifold structure shared between reference and spatial datasets. Building on this calibrated representation, BRIDGE imputes unmeasured genes using a multi-scale k-NN aggregation scheme, which reconstructs each spatial transcriptome from biologically coherent neighborhoods rather than unconstrained extrapolation. By decoupling calibration from latent embedding and performing prediction on a geometry-preserving representation, BRIDGE enables accurate and biologically meaningful completion of spatial transcriptomes across technologies, species, and tissues.

Across seven benchmark datasets, BRIDGE consistently showed superior or competitive performance relative to state-of-the-art approaches at both the gene- and cell-level, demonstrating robustness under diverse experimental and biological conditions. The linear calibration on shared genes enhanced cross-modality agreement and supported accurate prediction of unmeasured genes. Interpretability analysis further showed that the calibration matrix A and the gene-wise row-sum index R_g provide clear and directionally consistent signatures of gene-level adjustment. Applications to MERFISH mouse primary motor cortex and Xenium human breast cancer datasets highlighted BRIDGE's ability to recover spatial expression programs beyond the measured panels, identify previously inaccessible laminar patterns, and resolve B-cell and Stromal subtypes with distinct functional signatures and spatial niches. These findings illustrate that BRIDGE not only improves predictive accuracy but also expands the biological interpretability of imaging-based spatial transcriptomic data.

Despite its strengths, BRIDGE has practical considerations. As a reference-based method, it relies on the biological relevance and quality of the scRNA-seq reference for reliable anchor identification. Poorly matched references or anchors may introduce systematic errors. In practice, references sharing biological context and major cell populations with the spatial query support more stable anchor identification, particularly in heterogeneous systems. A general limitation shared by BRIDGE and existing spatial gene prediction methods lies in the evaluation protocol. Since ground-truth expression for unmeasured genes is unavailable in imaging-based spatial transcriptomics, performance is typically assessed by cross-validation on masked panel genes. While this provides a standardized and conservative basis for comparison, it may not fully reflect the difficulty of predicting truly unmeasured, lowly expressed genes. In addition, while shared genes are globally calibrated, reference-unique genes are not explicitly aligned to the spatial modality, which may introduce bias in their imputed expression. Finally, anchor identification via Seurat can be computationally expensive for large datasets. Importantly, because BRIDGE uses anchors as sparse constraints to learn a global calibration rather than as direct carriers of expression transfer, its performance is relatively insensitive to the precise anchor configuration, as supported by the anchor perturbation analyses. This robustness suggests that alternative, faster anchor discovery strategies (e.g. fastMNN [22]) or more aggressive reference subsampling schemes could be explored in practice to improve scalability, provided that major cell populations are preserved. These strategies would enable BRIDGE to scale more effectively to larger-scale datasets, facilitating application across a wide range of dataset sizes.

Future work may include extending the calibration framework to incorporate reference-unique genes, for example by introducing weak or regularized constraints that relate them to calibrated shared genes. Such constraints could leverage co-expression structure learned from the reference to anchor reference-unique genes indirectly, without requiring direct spatial measurements. Incorporating spatial context, such as neighborhood composition derived from spatial coordinates, also represents a natural extension for further refining prediction. Importantly, this information can be computed directly from spatial coordinates and cell identities already available in imaging-based assays, without requiring additional biological measurements. From a computational perspective, these spatial features would enter the framework as local weighting or regularization terms and are expected to add only modest overhead relative to anchor identification and nearest-neighbor search. Developing more scalable and reference-adaptive anchor discovery strategies remains an important direction. As spatial transcriptomics applications increasingly move toward three-dimensional tissue organization [48, 53], temporal or developmental dynamics [9, 62], and multimodal spatial measurements [71], future work may explore extending the BRIDGE framework to these emerging settings. For example, BRIDGE could be extended to three-dimensional spatial transcriptomics by incorporating 3D spatial structure into its calibration or neighborhood modeling, to temporal settings by accommodating time-dependent references, and to multimodal data by integrating additional molecular or imaging modalities within the same calibration framework. Together, these directions outline a modular roadmap in which future extensions operate at the calibration stage (e.g. incorporating reference-unique genes) as well as the neighborhood-based prediction stage (e.g. integrating spatial context), while preserving the overall structure, interpretability, and scalability of the BRIDGE framework.

Acknowledgements

This work was supported by the National Natural Science Foundation of China (Grant Nos. 12271198, 11871026), by the Fundamental Research Funds for the Central Universities (Grant Nos. CCNU25AI001, CCNU24JC004 and CCNU25JCPT029), by the Shenzhen Polytechnic University Research Fund (Grant No. 6025310025K) and by the Open Research Fund of Key Laboratory of Nonlinear Analysis & Applications (Central China Normal University), Ministry of Education, P. R. China (Grant No. NAA2025ORG003).

References

[1] N. J. Abbott, L. Rönnbäck, and E. Hansson, *Astrocyte-endothelial interactions at the blood-brain barrier*, Nat. Rev. Neurosci., 7:41–53, 2006.

[2] T. Abdelaal, S. Mourragui, A. Mahfouz, and M. J. Reinders, *SpaGE: Spatial gene enhancement using scRNA-seq*, Nucleic Acids Res., 48:e107, 2020.

[3] G. Bergers and S. Song, *The role of pericytes in blood-vessel formation and maintenance*, Neuro-Oncol., 7(4):452–464, 2005.

[4] N. A. Bhowmick, E. G. Neilson, and H. L. Moses, *Stromal fibroblasts in cancer initiation and progression*, Nature, 432:332–337, 2004.

[5] T. Biancalani et al., *Deep learning and alignment of spatially resolved single-cell transcriptomes with Tangram*, Nat. Methods, 18:1352–1362, 2021.

[6] L. Bod et al., *B-cell-specific checkpoint molecules that regulate anti-tumour immunity*, Nature, 619:348–356, 2023.

[7] M. Büttner, Z. Miao, F. A. Wolf, S. A. Teichmann, and F. J. Theis, *A test metric for assessing single-cell RNA-seq batch correction*, Nat. Methods, 16:43–49, 2019.

[8] D. Carrel, K. Hernandez, M. Kwon, C. Mau, M. P. Trivedi, L. M. Brzustowicz, and B. L. Firestein, *Nitric oxide synthase 1 adaptor protein, a protein implicated in schizophrenia, controls radial migration of cortical neurons*, Biol. Psychiatry, 77:969–978, 2015.

[9] A. Chen et al., *Spatiotemporal transcriptomic atlas of mouse organogenesis using DNA nanoball-patterned arrays*, Cell, 185:1777-1792.e1721, 2022.

[10] K. H. Chen, A. N. Boettiger, J. R. Moffitt, S. Wang, and X. Zhuang, *Spatially resolved, highly multiplexed RNA profiling in single cells*, Science, 348:aaa6090, 2015.

[11] S. Chen, B. Zhang, X. Chen, X. Zhang, and R. Jiang, *stPlus: A reference-based method for the accurate enhancement of spatial transcriptomics*, Bioinformatics, 37:i299–i307, 2021.

[12] C. Cheng, W. Chen, H. Jin, and X. Chen, *A review of single-cell RNA-seq annotation, integration, and cell-cell communication*, Cells, 12:1970, 2023.

[13] R. Dries, J. Chen, N. Del Rossi, M. M. Khan, A. Sistig, and G.-C. Yuan, *Advances in spatial transcriptomic data analysis*, Genome Res., 31:1706–1718, 2021.

[14] O. Elhanani, R. Ben-Uri, and L. Keren, *Spatial profiling technologies illuminate the tumor microenvironment*, Cancer Cell, 41:404–420, 2023.

[15] C.-H. L. Eng et al., *Transcriptome-scale super-resolved imaging in tissues by RNA seqFISH+*, Nature, 568:235–239, 2019.

[16] G. Faraco, L. Park, J. Anrather, and C. Iadecola, *Brain perivascular macrophages: Characterization and functional roles in health and disease*, J. Mol. Med., 95:1143–1152, 2017.

[17] G. Faraco et al., *Perivascular macrophages mediate the neurovascular and cognitive dysfunction associated with hypertension*, J. Clin. Investig., 126:4674–4689, 2016.

[18] E. N. Farah et al., *Spatially organized cellular communities form the developing human heart*, Nature, 627:854–864, 2024.

[19] I. Galea, *The blood-brain barrier in systemic infection and inflammation*, Cell. Mol. Immunol., 18:2489–2501, 2021.

[20] C. Gao, J. Jiang, Y. Tan, and S. Chen, *Microglia in neurodegenerative diseases: Mechanism and potential therapeutic targets*, Signal Transduct. Target. Ther., 8:359, 2023.

[21] L. Gao et al., *Single-neuron projectome of mouse prefrontal cortex*, Nat. Neurosci., 25:515–529, 2022.

[22] L. Haghverdi, A. T. Lun, M. D. Morgan, and J. C. Marioni, *Batch effects in single-cell RNA-sequencing data are corrected by matching mutual nearest neighbors*, Nat. Biotechnol., 36:421–427, 2018.

[23] Y. Hao et al., *Dictionary learning for integrative, multimodal and scalable single-cell analysis*, Nat. Biotechnol., 42:293–304, 2024.

[24] S. He et al., *High-plex imaging of RNA and proteins at subcellular resolution in fixed tissue by spatial molecular imaging*, Nat. Biotechnol., 40:1794–1806, 2022.

[25] M. Huan et al., *SAVER: Gene expression recovery for single-cell RNA sequencing*, Nat. Methods, 15:539–542, 2018.

[26] A. Janesick et al., *High resolution mapping of the tumor microenvironment using integrated single-cell, spatial and in situ analysis*, Nat. Commun., 14:8353, 2023.

[27] R. Kalluri, *The biology and function of fibroblasts in cancer*, Nat. Rev. Cancer, 16:582–598, 2016.

[28] E. S. Lein et al., *Genome-wide atlas of gene expression in the adult mouse brain*, Nature, 445:168–176, 2007.

[29] Y. Li et al., *Spatiotemporal transcriptome atlas reveals the regional specification of the developing human brain*, Cell, 186:5892–5909.e5822, 2023.

[30] G. C. Linderman, J. Zhao, M. Roulis, P. Bielecki, R. A. Flavell, B. Nadler, and Y. Kluger, *Zero-preserving imputation of single-cell RNA-seq data*, Nat. Commun., 13:192, 2022.

[31] Y. Liu et al., *Conserved spatial subtypes and cellular neighborhoods of cancer-associated fibroblasts revealed by single-cell spatial multi-omics*, Cancer Cell, 43:905–924.e6, 2025.

[32] S. K. Longo, M. G. Guo, A. L. Ji, and P. A. Khavari, *Integrating single-cell and spatial transcriptomics to elucidate intercellular tissue dynamics*, Nat. Rev. Genet., 22:627–644, 2021.

[33] R. Lopez, A. Nazaret, M. Langevin, J. Samaran, J. Regier, M. I. Jordan, and N. Yosef, *A joint model of unpaired data from scRNA-seq and spatial transcriptomics for imputing missing gene expression measurements*, arXiv:1905.02269, 2019.

[34] M. D. Luecken et al., *Benchmarking atlas-level data integration in single-cell genomics*, Nat. Methods, 19:41–50, 2022.

[35] R. Ma, E. D. Sun, D. Donoho, and J. Zou, *Principled and interpretable alignability testing and integration of single-cell data*, Proc. Natl. Acad. Sci. USA, 121:e2313719121, 2024.

[36] B. A. MacVicar and E. A. Newman, *Astrocyte regulation of blood flow in the brain*, Cold Spring Harb. Perspect. Biol., 7:a020388, 2015.

[37] X. Mao et al., *Crosstalk between cancer-associated fibroblasts and immune cells in the tumor microenvironment: New findings and future perspectives*, Mol. Cancer, 20:163, 2021.

[38] E. Martinis, S. Tonon, A. Colamatteo, A. La Cava, G. Matarese, and C. E. M. Pucillo, *B cell immunometabolism in health and disease*, Nat. Immunol., 26(3):366–377, 2025.

[39] V. Marx, *Method of the year: Spatially resolved transcriptomics*, Nat. Methods, 18:9–14, 2021.

[40] I. Mattiola, A. Mantovani and M. Locati, *The tetraspan MS4A family in homeostasis, immunity, and disease*, Trends Immunol., 42:764–781, 2021.

[41] K. R. Maynard et al., *Transcriptome-scale spatial gene expression in the human dorsolateral prefrontal cortex*, Nat. Neurosci., 24:425–436, 2021.

[42] B. F. Miller, D. Bambah-Mukku, C. Dulac, X. Zhuang, and J. Fan, *Characterizing spatial gene expression heterogeneity in spatially resolved single-cell transcriptomic data with nonuniform cellular densities*, Genome Res., 31:1843–1855, 2021.

[43] J. R. Moffitt et al., *Molecular, spatial, and functional single-cell profiling of the hypothalamic preoptic region*, Science, 362:eaau5324, 2018.

[44] A. V. Molofsky, R. Krencik, E. M. Ullian, H.-h. Tsai, B. Deneen, W. D. Richardson, B. A. Barres, and D. H. Rowitch, *Astrocytes and disease: A neurodevelopmental perspective*, Genes Dev., 26:891–907, 2012.

[45] R. Muñoz-Castañeda et al., *Cellular anatomy of the mouse primary motor cortex*, Nature, 598:159–166, 2021.

[46] A. M. Reimold, N. N. Iwakoshi, J. Manis, P. Vallabhajosyula, E. Szomolanyi-Tsuda, E. M. Gravallese, D. Friend, M. J. Grusby, F. Alt, and L. H. Glimcher, *Plasma cell differentiation requires the transcription factor XBP-1*, Nature, 412:300–307, 2001.

[47] J. Rustenhoven, D. Jansson, L. C. Smyth, and M. Dragunow, *Brain pericytes as mediators of neuroinflammation*, Trends Pharmacol. Sci., 38:291–304, 2017.

[48] M. Schott et al., *Open-ST: High-resolution spatial transcriptomics in 3D*, Cell, 187:3953–3972.e3926, 2024.

[49] H. Shi, Y. He, Y. Zhou, J. Huang, K. Maher et al., *Spatial atlas of the mouse central nervous system at molecular resolution*, Nature, 622:552–561, 2023.

[50] P. L. Ståhl et al., *Visualization and analysis of gene expression in tissue sections by spatial transcriptomics*, Science, 353:78–82, 2016.

[51] R. R. Stickels, E. Murray, P. Kumar, J. Li, J. L. Marshall, D. J. Di Bella, P. Arlotta, E. Z. Macosko, and F. Chen, *Highly sensitive spatial transcriptomics at near-cellular resolution with Slide-seqV2*, Nat. Biotechnol., 39:313–319, 2021.

[52] C. Su et al., *Single-cell RNA sequencing in multiple pathologic types of renal cell carcinoma revealed novel potential tumor-specific markers*, Front. Oncol., 11:719564, 2021.

[53] X. Sui et al., *Scalable spatial single-cell transcriptomics and translatomics in 3D thick tissue blocks*, Nat. Methods, 22:2574–2584, 2025.

[54] M. D. Sweeney, S. Ayyadurai, and B. V. Zlokovic, *Pericytes of the neurovascular unit: Key functions and signaling pathways*, Nat. Neurosci., 19:771–783, 2016.

[55] H. Tabata et al., *Erratic and blood vessel-guided migration of astrocyte progenitors in the cerebral cortex*, Nat. Commun., 13:6571, 2022.

[56] V. Thorsson et al., *The immune landscape of cancer*, Immunity, 48:812–830.e814, 2018.

[57] T. F. Tedder, J. C. Poe, and K. M. Haas, *CD22: A multifunctional receptor that regulates B lymphocyte survival and signal transduction*, Adv. Immunol., 88:1–50, 2005.

[58] D. Van Dijk et al., *Recovering gene interactions from single-cell data using data diffusion*, Cell, 174:716–729.e727, 2018.

[59] M. H. J. van Oers, S. T. Pals, L. M. Evers, C. E. van der Schoot, G. Koopman, J. M. G. Bonfrer, R. Q. Hintzen, A. E. von dem Borne, and R. A. W. van Lier, *Expression and release of CD27 in human B-cell malignancies*, Blood, 82:3430–3436, 1993.

[60] M. Vanlandewijck et al., *A molecular atlas of cell types and zonation in the brain vasculature*, Nature, 554:475–480, 2018.

[61] J. Venna and S. Kaski, *Neighborhood preservation in nonlinear projection methods: An experimental study*, in: Artificial Neural Networks – ICANN 2001, Lecture Notes in Computer Science, Vol. 2130, Springer, 485–491, 2001.

[62] X. Wei et al., *Single-cell Stereo-seq reveals induced progenitor cells involved in axolotl brain regeneration*, Science, 377:eabp9444, 2022.

[63] F. A. Wolf, P. Angerer, and F. J. Theis, *SCANPY: Large-scale single-cell gene expression data analysis*, Genome Biol., 19:15, 2018.

[64] S. T. Yang and X. F. Zhang, *ENGEP: Advancing spatial transcriptomics with accurate unmeasured gene expression prediction*, Genome Biol., 24:293, 2023.

[65] Y. Yang et al., *Pan-cancer single-cell dissection reveals phenotypically distinct B cell subtypes*, Cell, 187:4790–4811.e4722, 2024.

[66] Z. Yao et al., *A transcriptomic and epigenomic cell atlas of the mouse primary motor cortex*, Nature, 598:103–110, 2021.

[67] Z. Yao et al., *A taxonomy of transcriptomic cell types across the isocortex and hippocampal formation*, Cell, 184:3222–3241.e3226, 2021.

[68] Z. Yao et al., *A high-resolution transcriptomic and spatial atlas of cell types in the whole mouse brain*, Nature, 624:317–332, 2023.

[69] G. Yu, L. G. Wang, Y. Han, and Q. Y. He, *clusterProfiler: An R package for comparing biological themes among gene clusters*, OMICS J. Integr. Biol., 16(5):284–287, 2012.

[70] R. Zhan et al., *NAD^+ rescues aging-induced blood-brain barrier damage via the CX43-PARP1 axis*, Neuron, 111:3634–3649.e3637, 2023.

[71] D. Zhang et al., *Spatial epigenome-transcriptome co-profiling of mammalian tissues*, Nature, 616:113–122, 2023.

[72] M. Zhang, S. W. Eichhorn, B. Zingg, Z. Yao, K. Cotter, H. Zeng, H. Dong, and X. Zhuang, *Spatially resolved cell atlas of the mouse primary motor cortex by MERFISH*, Nature, 598:137–143, 2021.

[73] Y. Zhang, V. Petukhov, E. Biederstedt, R. Que, K. Zhang, and P. V. Kharchenko, *Gene panel selection for targeted spatial transcriptomics*, Genome Biol., 25:35, 2024.

[74] H. Zeng et al., *Large-scale cellular-resolution gene profiling in human neocortex reveals species-specific molecular signatures*, Cell, 149:483–496, 2012.

[75] X. Zhuang, *Spatially resolved single-cell genomics and transcriptomics by imaging*, Nat. Methods, 18:18–22, 2021.

[76] `https://github.com/BohanSi/BRIDGE`